國 立 中 央 大 學

物 理 學 系

碩 士 論 文

Search for heavy resonances decaying into a Z boson and a Higgs boson in the 2l2b final state in pp collisions at $\sqrt{s} = 13$ TeV

研 究 生：童宇軒

指導教授：余欣珊

中 華 民 國 一〇五 年 十二 月

Search for heavy resonances decaying into a Z boson and a Higgs boson in the $2l2b$ final state in pp collisions at $\sqrt{s}$ = 13 TeV

by

Yee Shian Henry Tong

Submitted to the Department of Physics
in partial fulfillment of the requirements for the degree of

Master of Physics

at the

NATIONAL CENTRAL UNIVERSITY

November 2016

Author . . . .

Department of Physics
April 21, 2017

Certified by . . . .

Shin-Shan Eiko Yu
Associate Professor
Thesis Supervisor

Accepted by . . . .

Yuan-Hann Chang
Professor
Chairman, Thesis Committee

Search for heavy resonances decaying into a Z boson and a Higgs boson in the $2l2b$ final state in pp collisions at $\sqrt{s}$ = 13 TeV

by

Yee Shian Henry Tong

Submitted to the Department of Physics
on April 21, 2017, in partial fulfillment of the
requirements for the degree of
Master of Physics

Abstract

A search for heavy resonances decaying to a Higgs boson and a Z boson is presented. The analysis is based on the data collected in 2015 with the CMS detector at a center-of-mass energy $\sqrt{s}$ = 13 TeV, corresponding to an integrated luminosity of 2.51 fb^{-1}. The Higgs bosons are reconstructed from high momentum $b\bar{b}$ quark pairs that are detected as a single massive jet, while the Z bosons are reconstructed from electron pairs and muon pairs. The analysis is separated in electron and muon channels, with single and double b-tag categories. A 95% upper limit on the production cross section of $\sigma_X \times \mathcal{B}(X \to ZH)$ is derived from the combination of four categories with a limit of 0.063 pb to 0.265 pb for m_X from 800 to 4000 GeV.

Thesis Supervisor: Shin-Shan Eiko Yu
Title: Associate Professor

摘要

本篇論文呈現了由新理論模型預測之粒子衰變到一個希格斯粒子和一個 *Z* 玻色子的分析。本分析使用了於 2015 年由大強子對撞機中的緊湊渺子線圈偵測器所記錄之質子-質子對撞總能量為 13 TeV，總亮度為 2.5 fb^{-1} 的數據。高動量的希格斯粒子衰變到一個底夸克和一個反底夸克，在偵測器裡被偵測為一個大質量的噴流。*Z*玻色子有兩個衰變通道，分別為正反電子通道以及正反渺子通道。本分析將分別探討電子通道和渺子通道，各通道將再細分為單底夸克標記和雙底夸克標記此二類別。通過合併電子通道和渺子通道，以及它們所有的底夸克標記類別，結果顯示質量由 800 GeV 至 4000 GeV 的新粒子於 95%信置區間的生產截面上限為 0.063 *pb* 至 0.265 *pb*。

Contents

List of Figures

List of Tables

Chapter 1

Introduction and Theory Overview

1.1 Introduction

1.2 Theory

The discovery of the boson whose mass around 125 GeV and with properties close to Higgs mechanism in the Standard model has incited the search under Higgs potential including Higgs self-coupling. Especially, it is a worth explored channel to finding new physic beyond Standard model. Targeting heavy resonance, the model Wraped Extra Dimension is considered.

1.2.1 Wraped Extra Dimension

1.2.2 Motivation

There are models predicting heavy resonances decaying into VV. Several researches on these channels are performed in both CMS and ATLAS. There are also the combinations of these analyses. The combination from ATLAS excludes the resonance of Bulk Graviton from below 810 GeV, and despit the combination from CMS fails to exclude any mass spectum of Bulk Graviton given a less sensitive model, it sets the upper limit of 10 fb of cross section of Bulk Graviton through M_X from 600 to 2500 GeV. Besides, searches for Bulk Graviton decaying into HH in four b-flavored quarks final state have been perfromed by CMS and ATLAS at $\sqrt{s}$ = 8 TeV. They exlude the mass region below 830 and 720 GeV respectively. The intermediate region of the mass of heavy resonances ($M_X \approx 2$ TeV) is left interesting to be explored.

Chapter 2

Collider and Detector

2.1 Large Hadron Collider

Large Hadron Collider locates at Geneva region about 100 meters underground which is built and operated by European Organization for Nuclear Research, CERN. Its circumference is 27-km-long, and its two proton beams in which the energy of each proton is 7 TeV produce collisions at center-of-mass energy reaching 13 TeV in 2015, which makes it both the largest in size and highest center-of-mass energy collider in the world. Besides, LHC also provides heavy-ion collision to include the study of the behavior of quantum chromo dynamics, QCD, under high density parton mementum fraction. When it operates, the intervals between proton bunch crossing is 25 ns, that is to say, 10^9 events are produced per second. Besides, an average of 20 unelastic collision will be produced in a signle bunch crossing. It is undoubtly challenging requirement on techique not only to reduce the number of events recorded by triggers but also to alleviate the effect by unelastic vertex of pile-ups.

2.2 The Compact Muon Solenoid Detector

As one of the detectors of the LHC, the Compact Muon Solenoid Detector, CMS, shares the same aims of the LHC. Basically, it will elucidate the phsical properities of the Higgs boson whose mass is around 125 GeV, and it will also test the mathimatical consistency of Standard Model, SM, at TeV scale. People also hope to find the new physic beyond SM where Supersymmetry and Extra Dimension is often being considered. The latter nessisates the finding of the Graviton in TeV scale. All researches need a delicate disign of a detector, including good charged particle reconstruction to trace the vertex, good EM energy resolution, and good measurement on missing transverse energy and di-jet reslotion.

- The tracker: The high granularity tracker at inner detector can well reconstruct the trace of charged particles. It is also indispensible for indentifying b-flavored jets and τ.

- The muon chamber: The muon chamber combined with tracker information under the magnetic field of opposite direction can together interpolate to reduce mis-matching rate in muon reconstruction and identify the cosmic muons from outside of the detector.

- The calorimeters: The calorimeters facilitate the shower and measure the energy of post-shower particles. The information will further be clustered into the energy corespoding to their mother particles.

2.2.1 Detector Kinematics

To better describe the geometry of the detector, a set of axes is set. The z axis is along the beam lime, and the positive direction points to counter-clockwise direction of the beam pipe. The xy plane is perpendicular to z axis and can be described by ϕ:

$$x = cos\phi, y = sin\phi, \tag{2.1}$$

where ϕ is the azimuthal angle. The variable rapidity y is used to describe the angle θ between one vetcor and the z axis. Pseudorapidity is more convinent to use instead of rapdity, because it is invariant under boosts along the longitudinal axis. Pseudorapidity is defined as the rapidity for a massless particle whose $E \approx |\vec{p}|$.

$$y = \frac{1}{2}ln(\frac{E+p_z}{E-p_z}), \eta = \frac{1}{2}ln(\frac{|\vec{p}|+p_z}{|\vec{p}|-p_z}) = -log[tan(\theta/2)] \tag{2.2}$$

2.2.2 Magnet System

In order to have a resolution for charged particles in the tarckers, magnetic field must maintain to bend the tracks of charged particles. Providing the magnetic field of CMS, the superconducting solenoid is installed between the calorimeters and muon chambers with diameter of 6.3 m, length of 12.5 m, and mass of 200 t. Designed to have 4 T magnetic field at the center of the detector, the solenoid uses four layers based on the Ampere-turn (41.7MA-turn) and made of aluminum alloy. The width of one layer is far less than its counterpart of other detectors, and its lower limit is restricted by the magnetic pressure and the material properity of aluminum. It also breaks the convention, for that the magnetic stress is shared between itself and the the outer mandrels. The yoke is composed of five barrel wheels and 6 endcap disks. Besides, to avoid the "quench back" effect, where the ebb currents induced in outer mandrels heat up the coil above superconducting critical temperature, a proctecting circuit is designed and worked by either fast discharge or slow discharge throungh dumping.

2.2.3 Tracker Detector

Having precise reconstructed parimary and secondary verteces, the Tracker detector is designed to be at innerest part of the CMS detector. It needs to be fast enough to collect data between 25 ns interval of bunch crossing and high granularity enough to indentify the trajectories. Two kinds of tracker detector are used for difference purpose, the pixel trackers and the strip trackers. While the former is better at determining three dimensional space and at enduring the radiation dose, the latter covers larger total erea since it costs less per area. There are three cylindrical pixel detectors at radii of 4.4, 7.3 and 10.2 cm and two disks of piexl detectors at |z| of 34.5 and 46.5 cm on each side of the interaction point. They together give coverage to pseudorapidity $|\eta| < 2.5$ and an area of about 1 m^2 with total 66 million pixels whose size is 100 $\times$ 150 μm^2. The strip detectors are seperated into several subsystems. The Tracker Inner Barrel and the Tracker Inner Disk (TIB/TID) at radii extending to 55 cm together, composing 4 layers and 3 disk on each side, provide four $r - \phi$ measurements with resoultion 23 μm and 35 μm by the first two layers and the others respectively. Tracker Outer Barrel (TOB) ranges toward radius of 116 cm and performs six $r - \phi$ measurements with resoultion 53 μm and 35 μm by the first four layers and the others respectively. In addition, Tarcker EndCap (TEC) gives another 9 measurements on ϕ by its nine layers installed at 124 cm $<$ |z| $<$ 282 cm.

Pixel Trackers

The pixel trackers are constitued by pn-junctions operated in depletion. When particles pass depletion zone, induced electron-hole pairs will produce signal current and further be amplfied and read out. To take the high density radiation dose into account, a n+-doped electrodes in n-doped substratrate design is chosed as sensor. Another advantage of the n-on-n concept is that a guard ring can be made around the sensor to prevent voltage break-down in air (1.2V/μm). The isolation between electrode prevents electrodes from shortening after radiation. Open p-stop and moderate p-spary are isolation designs inplemented on disks and barrel respectively.

Strip Trackers

The elements in the trackers are single-side p-on-n silicon micro-strip sensors. Besieds, the six inch wafers are used instead of four inch wafers to reduce the cost. As the bulit-on surface charge of $\langle 100 \rangle$ crystal orientation of n substratrate is smaller than $\langle 111 \rangle$ one, the $\langle 100 \rangle$ is chosed to maintain the capacitance after irradiation.

2.2.4 Electromagnetic Calorimeter

The electromagnetic calorimeters, ECAL, is used to measure the energy of electromagnetic, EM, particles through EM shower. In the other hand, they can reconstruct the mother particles of electrons and photons indirectly. The system composes the ECAL Barrel (EB) in $|\eta| < 1.479$ and the ECAL Endcap (EE) in $1.479 < |\eta| < 3.0$. Lead-tungstate crystals (PbWO4) are chosed as scintillator where shower happens. Its short Radiation length (0.89cm) and Moliere radius (2.2cm) is appropriate for compact space in CMS. The photon detectors are set on the back on each crystal. Avalanche photodiodes are used for EB, while vacuum phototriodes are used for EE. Besides, the preshower detector (ES) is installed in front of the EE where $1.653 < |\eta| < 2.6$. There are two layers: lead radiators and silicon strip sensor. The EE is mainly used to identify π^0 and assists the identification of electrons against minimum ionizing particles.

2.2.5 Hadron Calorimeter

The hadron calorimeters measure the energy of hadrons, and they are substantial to detect the neutrinos or exotic particles by measrueing missing transverse energy. There are four subsystems including the barrel (HB) , the endcap (HE) , the outer (HO) , and the foward (HF) designs. Both the HB and the HE are sample detectors. The HB covers $|\eta| < 1.3$, while the HE covers $1.3 < |\eta| < 3$. They are both designed to consist of scintillators interleaved between brass (70% copper and 30% zink) absorbers beacause of high density of brass. Six brass layers of 50.5 mm, eight brass layers of 56.5 mm along with front and back plate of 40 and 75 mm give totally 87cm thickness of absorders in barrel, while the thickness of abosrbers in endcap is 79mm for each layer. The HB is not thick enough to contain all the energy of high energy particles. Thus, the HO is installed outside the HB to catch the rest of the later showers combined with the HB to give about 11.8 absorption lengths in total. In addition, to detect the very foward jets thus to improve the measurements of missing transverse energy, the HF is needed whose coverage extends to about $|\eta| = 5$. As the energy deposit is not uniformly distributed in the detector, the forward region takes higher radiation dose. The HF must be most radiontion-hard by means of the shielding including 40 cm steel, 40 cm concrete, and 5cm of polyethylene.

2.2.6 Muon Detector

Muon idenification ensures the measurement on expected background rate. For example, backgrounds whose the final state including one Z boson decaying into di-muons. This is essential for discovery of Higgs mechianism where backgound of ZZ is domiant. Besides, some physic beyond Standard Model, Super-Suymmertry for example, has muon in its final state. The CMS muon system is made up of three kinds of gaseous chamber detectors. First, the barrel drift tube (DT) chambers contain four layers distributing between $|\eta|$ <1.2. The first three layers include 12 chambers, eight for $r - \phi$ measurements and four for $|z|$ measurements, while the last layer only measures $r - \phi$. With a width of single cell of 42 mm, the maximum drift distance is its half, which has 380 ns maximum drift time. The cells filled with 85% Ar and 15% CO_2 set up an electrical field by 3600V anode wire at the central, 1800V two electrode strips at the ceil and the floor, and two 1800V cathode strips on each side. Second, the cathode strip chambers (CSC) have 6 layers and are grouped in 4 stations. Their fast response is suitable for more non-uniform magnetic field and more muons passing through in forward region, so they are placed $0.9 < |\eta| < 2.4$. The CSC disks are seperated into strips by either 20° or 10° in ϕ. Each chamber has 6 gas gaps with anode wires seperated by 7 cathode panels. The cylindrical wires make the r-coordinate measurements, while the charges induced on the strips interpolate to determine ϕ coordinate. The gas mixture is 40% Ar + 50% CO_2 +10% CF_2. Last, the resistive plate chambers (RPC) with fast response are added to muon system to complement the time resolution, especially with multiple-muon events. However, they have to work with DT and CSC, for RPC has less space resolution than the others do. There are two layers in each station for the first two stations of DT and one layer in each staion for the other two staions. In addition, three disks in the fisrt three CSC to improve the time resolution are used in determination of time of bunch crossing and muon p_T reconstruction. A module consists of 2 gaps in which there is a gas plate holded by two bakelites, referred as the up gap and the down gap with a strip between them connecting to the read-out . The triggers in muon system using RPC information can perform at high rate and a rahter high p_T of muons threshold.

2.3 The trigger system

The interval between bunch crossing in LHC is 25 ns which corresponds to a rate of events of 40 MHz. The trigger system is required to reduce the rate of events to be possible for recoding. The system is worked by Level-1 Trigger system (L1) and High-Level Trigger (HLT) togerther. The L1 Trigger will reduce at least to 100 kHz, and the HLT will then reduce to a maximum of 30kHz. The L1 Trigger is made up of several hardware progarmmable electrons which collect information from muon system and calormeters. On the other hand, the HLT triggers are software-like triggers which have the access to the readout of data. Thus, they are able to do the complex calulation similar to those done in the analysis off-line. The algorithm of HLT will be improved through the time.

Chapter 3

Analysis Strategy

The target of the analysis is to search for the heavy resonances decaying to di-Higgs where mass of heavy resonances is above 800 GeV. Each Higgs boson is assumed to further decay to $b\bar{b}$ and is reconstructed in a boosted jet including two b-flavored-like sub-jets by anti-kT08 algorithm. Higgs identification is done by selection on PUPPI soft-drop mass, N-subjetness, and double b-tagger.

3.1 Data and Simulated Samples

The analysis is preformed based on the data collected in pp collision with the CMS detector at $\sqrt{s}$ = 13 TeV. The integrated luminosity is $35.9 fb^{-1}$. Runs in which the detector normally operates was chosen according to the golden JSON file: $Cert\_271036 - 284044\_13TeV\_23Sep2016ReReco\_Collisions16\_JSON.txt$. The samples of data are listed in table 3.1.

3.2 Monte Carlo Simulation

The Monte Carlo, MC, simulations in the analysis are bulk graviton, radion, and multijet events. Bulk graviton, radion are used for setting the upper limit of cross section, while multijets events are used for testing the background estimation method and not used for final results. The names and the number of events of samples are listed in the table 3.2-3.4. The cross section of signal used in the final

Dataset	Processing	Int. lumi. (fb^{-1})
JetHT/Run2016B	23Sep2016	5.9
JetHT/Run2016C	23Sep2016	2.6
JetHT/Run2016D	23Sep2016	4.4
JetHT/Run2016E	23Sep2016	4.1
JetHT/Run2016F	23Sep2016	3.2
JetHT/Run2016G	23Sep2016	7.7
JetHT/Run2016H	PromptReco	8.9
Total		35.9

TABLE 3.1: List of datasets used in the analysis and its corresponding integrated luminosity in pp collision at $\sqrt{s}$ = 13 TeV.

results are listed in the table 3.5. Since the distributions of pile-ups of data and of MC are different, a pile-up re-weighting is applied to MC samples. Here the distribution of pile-ups of data is derived by using minibias cross section of pp collision of 69.2 mb.

Samples	σ(pb)	Events
BulkGravTohhTohbbhbb_narrow_M-1000_13TeV-madgraph	2.66	50000
BulkGravTohhTohbbhbb_narrow_M-1200_13TeV-madgraph	0.95	50000
BulkGravTohhTohbbhbb_narrow_M-1400_13TeV-madgraph	0.37	50000
BulkGravTohhTohbbhbb_narrow_M-1600_13TeV-madgraph	0.18	50000
BulkGravTohhTohbbhbb_narrow_M-1800_13TeV-madgraph	0.084	48400
BulkGravTohhTohbbhbb_narrow_M-2000_13TeV-madgraph	0.041	50000
BulkGravTohhTohbbhbb_narrow_M-2500_13TeV-madgraph	0.007	50000
BulkGravTohhTohbbhbb_narrow_M-3000_13TeV-madgraph	0.0017	50000

TABLE 3.2: List of bulk graviton $\rightarrow$ HH $\rightarrow$ $b\bar{b}$ Monte Carlo simulation and its corresponding cross section and the number of events. The cross sections are used in McM process at leading order, LO, and not used in the final results.

3.3 Event Reconstruction and Selection

To reduce the impact from both cosmic particles and noise of calorimeters, missing transverse energy, MET, filters are applied. If all particles are detected and

Samples	σ(pb)	Events
RadionTohhTohbbhbb_narrow_M-1000_13TeV-madgraph	1318	50000
RadionTohhTohbbhbb_narrow_M-1200_13TeV-madgraph	116.2	50000
RadionTohhTohbbhbb_narrow_M-1400_13TeV-madgraph	67.97	50000
RadionTohhTohbbhbb_narrow_M-1600_13TeV-madgraph	41.74	50000
RadionTohhTohbbhbb_narrow_M-1800_13TeV-madgraph	26.57	50000
RadionTohhTohbbhbb_narrow_M-2000_13TeV-madgraph	17.43	50000
RadionTohhTohbbhbb_narrow_M-2500_13TeV-madgraph	6.646	50000
RadionTohhTohbbhbb_narrow_M-3000_13TeV-madgraph	1.519	50000

TABLE 3.3: List of radion $\rightarrow$ HH $\rightarrow$ $b\bar{b}$ Monte Carlo simulation and its corresponding cross section and the number of events. The cross sections are used in McM process at LO and not used in the final results.

Samples	σ(pb)	Events
QCD_HT-100to200	2.785×10^7	81,906,377
QCD_HT-200to300	1.717×10^6	18,752,566
QCD_HT-300to500	3.513×10^5	20,312,907
QCD_HT-500to700	3.163×10^4	19,755,616
QCD_HT-700to1000	6831	15,595,234
QCD_HT-1000to1500	1207	4,966,123
QCD_HT-1500to2000	119.9	3,964,488
QCD_HT-2000toInf	25.24	1,984,407

TABLE 3.4: List of multijet Monte Carlo simulation and its corresponding cross section and the number of events. The cross sections are used in McM process at LO.

well-reconstructed in the detector, the sum of transverse momentum will be zero. However, if there are noise, ill-reconstructed particles or jets, the sum of transverse momentum will not equal to zero, and the negative of its value is defined as MET. The filters remove most events having anomaly MET based on different information given from the detectors. All filters used are listed in table 3.6.

After passing MET filters, at least one reconstructed pp collision vertex which passes following criteria is required in an event.

- Number of degree of freedom > 4

M_X(GeV)	σ(pp$\rightarrow X_G \rightarrow$HH) (fb)	σ(pp$\rightarrow X_R \rightarrow$HH) (fb)
750	2.408	155.46
800	1.771	128.68
900	0.953	88.433
1000	0.559	62.057
1500	0.057	12.897
1800	0.018	5.6664
2000	9.03E-03	3.3868
2500	1.86E-03	1.0193
3000	3.03E-04	0.3280
3500	1.15E-04	0.1114
4500	8.91E-06	1.26E-02

TABLE 3.5: List of the cross section $\times$ the branch ration of HH decay in fb. The model $k/\bar{M}_{Pl}$ = 0.1 in bulk graviton is considered, and the model Λ_R = 3TeV and kl = 35 of radion is considered.

Triggers
primary vertex filter
beam halo filter
HBHE noise filter
HBHE iso noise filter
ECAL TP filter
ee badSC noise filter
Bad PF Muon Filter
Bad Charged Hadron Filter

TABLE 3.6: List of MET filters applied in the analysis.

- Absolute displacement from the beamspot position along the z direction $<$ 24 cm
- Absolute displacement from the beamspot position along the transverse direction $<$ 2 cm

For the final state is all-hadronic, lepton veto is implemented. The event will be vetoed either if there is a tight-tagged muon or electron, or if there are two loose-tagged mouns or electrons with opposite charged.

3.3.1 Higgs Jet Reconstruction

Each candidate of particles is reconstructed with Particle-Flow, PF, algorithm in CMS by all the detector components. In the algorithm, priority of reconstruction form high to low are: muons, electrons, photons, charged hadrons, and neutral hadrons.

The jets are clustered with anti-k_T algorithm by PF candidates. Anti-k_T algorithm is done described below:

$$\begin{aligned} d_{ij} &= min(k_{ti}^{2p}, k_{tj}^{2p})\frac{\Delta_{ij}^2}{R^2} \\ d_{iB} &= k_{ti}^{2p}, \end{aligned} \tag{3.1}$$

where $\Delta_{ij}^2 = (y_i - y_j)^2 + (\phi_i - \phi_j)^2$, and k_{ti}, y_i, and ϕ_i are the transverse momentum, rapidity, and azimuth of particle i. The value of p is set according to the algorithm. The anti-k_T algorithm uses p = -1. Considering minimum term of k_t^{2p} between one hard particle and the selected soft particle compared to that between the soft particle and another soft particle, the former will be smaller because while the transverse momentum of hard particles is larger, its inverse square is smaller. Therefore, d_{ij} of the former is shorter, that is, a soft particle is more likely to cluster with hard particle around it. As a consequence, if there is no other hard particle within the range 2R of a hard particle, it will cluster a conical jet with all soft particles within range R. In other situation where the distance of two hard particles is between R and 2R, one can show that the particle having larger transverse momentum will cluster a conical jet, while the other is partly conical. Last, where distance of two hard particles $<$ R, two particles will merge into single jet. In the analysis, the jets is clustered using anti-k_T with range parameter R set to 0.8 (refrred as AK8 jets).

In one bunch crossing, the vetex having highest energy called primary vertex, and the others are called pile-ups, PUs. PUs may contribute some components in jet clustering which do not origninally belong to them. We can mitigate the effect by PUPPI algorithm, which is described below: First, a shape α_i of a particle i is defined:

$$\alpha_i = log \sum_{j \in event} \xi_{ij} \times \Theta(\Delta R_{ij} - R_{min}) \times \Theta(R_0 - \Delta R_{ij}) \\ \xi_{ij} = \frac{p_{Tj}}{\Delta R_{ij}}, \tag{3.2}$$

where Θ is the Heaviside step function, p_T is the transverse momentum, and ΔR_{ij} is the distance between particle i and j in $\eta\phi$ space. Hence, only particles falling in the cone size R_0 but not closer than R_{min} contribute to α. R_0 represent the locality of a jet, and R_{min} is most restricted by resolution of the detector. Then we seperate events into two cases: with and without tracker information. The former is used to weight the charged particles in central region, while the latter is used for charged particles in forward region and neutral particles. An addition scale factor depending on rapidity is applied to forward region. The calculation of weight uses the quantities of the median and the left-side RMS of α distribution. Finally, the weight of a particle is:

$$\chi_i^2 = \Theta(\alpha_i - \bar{\alpha}_{PU}) \frac{(\alpha_i - \bar{\alpha}_{PU})^2}{\sigma_{PU}^2}, \\ \omega_i = F_{\chi^2, NDF=1}(\chi_i^2), \tag{3.3}$$

where F_{χ^2} is the cumulative distribution function of the χ^2 distribution. One can find that if α of a particle less than the median, it will be considered from PU, and the step function in the first equation gives it a value of zero, while if α greater than the median, the value of χ^2 is close to one.

Basic selection is applied on AK8 jet. We only consider the jets having the largest and the second largest transverse momentum in an event. The p_T of the jets must greater than 300 GeV and pseudorapidity $|\eta|$ must less than 2.4. Also, the tight PF jet identification provided by JETMET group is required, which is summarized in the table 3.7, where fraction are referring to energy fraction, and constituents and multiplcity are referring to the number of particles.

Variable	Cut
Neutral hadron fraction	< 0.9
Neutral EM fraction	< 0.9
Charged EM fraction	< 0.9
Number of Constituents	> 1
Muon fraction	< 0.8
Charged hadron fraction	> 0
Charged Multiplicity	> 0

TABLE 3.7: List of the tight PF jet identification.

3.3.2 Heavy Resonance Seletion

The difference between two $|\eta|$ of two leading jets of signal events will be less than that of multi-jet events because the Higgs jets are from heavy resonance decay resulting in two jets close to each other, and yet the $|\eta|$ of the jets in multi-jet events are uniformly distributed. To reduce the contribution from multi-jet events, which are our mainly source of background, we require a $|\Delta\eta|$ cut on < 1.3. Next, We target the heavy resonances whose mass is above 800 GeV. Therefore, a revised mass of heavy resonances is also required. The mass of heavy resonances, M_{jj}, is get from sum of four momenta of two Higgs jets. A revised mass is used to narrow the width and correct the peak position of the M_{jj} distribution, referred as "reduced mass" for the following chapters.

$$M_{jj}^{reduced} = M_{jj} - (M_{j1} - M_H) - (M_{j2} - M_H), \tag{3.4}$$

where M_{j1} or M_{j2} is the mass of Higgs jets, and M_H is the mass of physic Higgs boson. The reduce mass is required to be greater than 750 GeV.

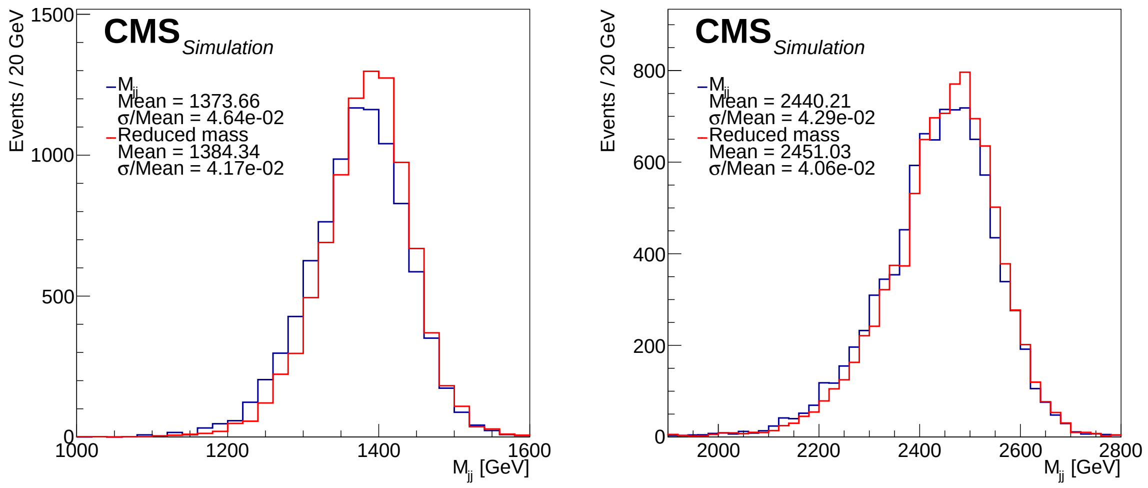

FIGURE 3.1: The comparison of M_{jj} and reduced mass distribution of bulk graviton M_X = 1.4 (left) and 2.5 TeV (right). The mean and the σ/mean of a Gaussian fit to the distribution are shown.

3.3.3 Higgs Tagging Seletion

The soft-drop procedure is inplemented to re-cluster the jet by removing soft contribution as follow:

- Deculster a targeted jet into two sub-jets.
- Continue to decompose the sub-jets until the condition is achieved

$$\frac{min(p_{T1}, p_{T2})}{p_{T1} + p_{T2}} > Z_{cut} \times (\frac{\Delta R_{12}}{R_0})^{\beta}, \quad (3.5)$$

  where R_0 is the cone size of the original cluster algorithm, p_T are the transverse momenta of two sub-jets, ΔR_{12} is the distance of two sub-jets in $\eta\phi$ space, and Z_{cut} and β are parameters.

- The unsplit singelet particle at the end will either be removed or remain preserved.

If $\beta > 0$, the soft contribution is removed while remain a fraction of soft-collinear radiation. If $\beta < 0$, soft drop removes both soft and collinear radiation. In CMS, the Z_{cut} and β are set 0.1 and zero respectively. The difference between the peak of the distribution of mass of PUPPI soft-drop jets and the mass of physical Higgs boson is found. A Correction is applied to move the peak to the true phyiscal value. The ratio is derived by peak of the mass distribution of reconstructed jets in WW dijet Monte Carlo simulations to mass of true physical value. The corrected PUPPI soft-drop mass of the first two leading jets are required between 105 and 135 GeV, which has been optimized.

The ratio τ_N to τ_{N-1} is used as a discriminant to seperate the boosted events decaying into N particles from multi-jet events. τ_N is so-called "N-subjettiness" algorithm:

$$\tau_N = \frac{1}{d_0}\sum_k p_{T,k} min\{\Delta R_{1,k}, \Delta R_{2,k}, \cdots, \Delta R_{N,k}\}$$
$$d_0 = \sum_k p_{T,k} R_0, \tag{3.6}$$

where k runs over the constituent particles in a given jet, ΔR_{jk} is the distance between particle j and k in $\eta\phi$ space, R_0 is the cone size of the original cluster algorithm. In the analysis, the boosted jets are decaying into two sub-jets, so τ_2 to τ_1 ratio is used, and it is referred as τ_{21} in the following chapters. The τ_{21} is required to be less than 0.55. The working point and simualtion-to-data scale factor is derived by JME POG.

The double-b tagger is a multiple variable analysis discriminant used to identify b-flavor jets. Jets in multi-jet evetns and Higgs jets decaying into $b\bar{b}$ are used for training. Here lists out the input information:

- The first four impact paramters to its uncertainty values ordered from the largest to the smallest.
- The N-subjettiness axes referred as τ-axes use the information of N-subjettiness
- The first two impact parameters to its uncertainty values of τ-axes ordered from the largest to the smallest.

- The meausured significance of impact parameters of the first two tracks whose mass of secondary vertex is above buttom quark threshold.
- The number of secondary verteces of the jet.
- The significance of two dimenisional distance between the primary vertex and the secondary vertex and flight distance of the secondary vertex with smallest three dimenisional distance uncertainty for each τ-axes.
- ΔR of the two secondary verteces with smallest three dimenisional distance uncertainty for each τ-axes.
- The τ-axis of the two secondary verteces with smallest three dimenisional distance uncertainty for each τ-axes.
- The sum of the mass of the secondary verteces associated to the τ-axis for each τ-axes.
- The sum of energy of secondary verteces associated to the τ-axis for each τ-axes.
- The relative pseudorapidity of three tracks of leading secondary vertex with respect to their τ-axis for each τ-axes.
- The sum of energy of all tracks in the AK8 jet.
- The z variable, defined as:

$$z = \Delta R(SV_0, SV_1) \times \frac{p_{T,SV_1}}{m(SV_0, SV_1)}, \tag{3.7}$$

  where SV_0 and SV_1 are the secondary verteces with the smallest 3D flight distance uncertainty.

The double-b working points and simualtion-to-data scale factor is derived by BTV POG. The analysis is seperated into two catgory with two Higgs jets in the events either both passing loose working point (> 0.3) or both passing tight working point (> 0.8), which are referred as LL and TT categories respectively.

3.4 Triggers

Since the final state includes di-Higgs jets, the triggers are selected considering the requirements on the scale sum of the energy of external partons H_T, $|\Delta\eta$(the first two leading jets)$|$, M_{jj}, p_T, the groomed mass of the jets, and double-b tagger. PFHT900 is used to supplement the inefficiency of PFHT800 in period H of data taking.

Triggers
HLT_PFHT800
HLT_PFHT900
HLT_PFHT650_WideJetMJJ900DEtaJJ1p5
HLT_AK8PFJet360_TrimMass30
HLT_AK8DiPFJet280_200_TrimMass30_BTagCSV_p20
HLT_AK8PFHT650_TrimR0p1PT0p03Mass50

TABLE 3.8: List of Triggers applied in the analysis.

3.5 Simulation Distribution

In the section, distribution of Monte Carlo simulations of signal and background will be shown to demonstrate the discrimination of each variables of the selection. For each distribution, all selection described in previous section is required except the variable itself and double-b tagger discriminant. The cross section of every signal is set to 20 pb. The numbers of events of signal and of background are normalized to same luminosity of data of 35.9fb^{-1}. Multi-jet events are added up by samples of different H_T section listed in table 3.4, and seperated into four categories summarized in the table 3.10. Besides, the cross sections at

Selection	Requirement
Number of good vertex	> 1
MET Filters	AND of all filters
Trigger	OR of all triggers
Lepton veto	one tight-tagged or two loose-tagged
p_T of AK8 jets	> 300GeV
$\vert\eta\vert$ of AK8 jets	< 2.4
Tight LepVeto jet ID	pass
$\vert\Delta\eta$ (two AK8 jets) $\vert$	< 1.3
Reduce mass	> 750 GeV
corrected PUPPI soft-drop mass	$105 <$ and < 135
τ_{21}	< 0.55
double-b tagger	> 0.3 (LL) or > 0.8 (TT)

TABLE 3.9: List of all selection in the analysis.

M_X	Trig.	Jet p_T, η	Veto$_{lep}$	$\Delta\eta$	Lepton	τ_{21}	M_{AK8}	M_{jj}^{red}	LL	TT
750	0.432	0.248	0.247	0.213	0.213	0.093	0.029	0.024	0.016	0.009
800	0.547	0.367	0.367	0.327	0.326	0.152	0.051	0.050	0.036	0.021
900	0.693	0.552	0.552	0.487	0.485	0.245	0.083	0.083	0.061	0.033
1000	0.772	0.666	0.666	0.552	0.550	0.296	0.101	0.101	0.075	0.041
1200	0.859	0.792	0.792	0.585	0.584	0.335	0.116	0.116	0.084	0.044
1400	0.902	0.854	0.854	0.591	0.590	0.355	0.123	0.123	0.087	0.044
1600	0.928	0.890	0.889	0.592	0.591	0.358	0.124	0.124	0.086	0.041
1800	0.946	0.913	0.913	0.595	0.594	0.365	0.124	0.124	0.082	0.036
2000	0.957	0.931	0.931	0.598	0.598	0.365	0.127	0.127	0.081	0.036
2500	0.975	0.956	0.955	0.596	0.595	0.367	0.125	0.125	0.076	0.030
3000	0.981	0.966	0.965	0.589	0.589	0.357	0.123	0.123	0.068	0.022
3500	0.987	0.973	0.972	0.582	0.582	0.349	0.116	0.116	0.059	0.018
4500	0.991	0.977	0.976	0.579	0.578	0.334	0.103	0.103	0.044	0.010

TABLE 3.10: The cut flow of all M_X (GeV) of spin-0 radion.

leading order of multi-jet events are multiplied by a factor about 0.7 to modify them closer to the value of next leading order.

M_X	Trig.	Jet p_T, η	Jet ID	$\Delta\eta$	Veto$_{lep}$	τ_{21}	M_{AK8}	M_{jj}^{red}	LL	TT
750	0.610	0.368	0.368	0.331	0.330	0.149	0.049	0.039	0.027	0.015
800	0.758	0.541	0.541	0.503	0.502	0.237	0.080	0.079	0.057	0.032
900	0.903	0.772	0.771	0.716	0.715	0.371	0.125	0.124	0.092	0.051
1000	0.958	0.885	0.885	0.801	0.799	0.434	0.151	0.151	0.111	0.062
1200	0.988	0.962	0.961	0.843	0.842	0.499	0.178	0.178	0.129	0.068
1400	0.996	0.984	0.983	0.854	0.853	0.524	0.182	0.182	0.129	0.064
1600	0.998	0.993	0.993	0.858	0.857	0.532	0.186	0.186	0.128	0.061
1800	0.999	0.996	0.996	0.864	0.863	0.543	0.193	0.193	0.130	0.059
2000	1.000	0.998	0.998	0.861	0.860	0.541	0.190	0.190	0.123	0.054
2500	1.000	0.999	0.999	0.862	0.862	0.538	0.188	0.188	0.113	0.044
3000	1.000	1.000	0.999	0.865	0.865	0.530	0.186	0.186	0.102	0.034
4000	1.000	1.000	0.999	0.861	0.861	0.505	0.166	0.166	0.078	0.021
4500	1.000	1.000	0.999	0.859	0.858	0.502	0.156	0.156	0.065	0.016

TABLE 3.11: The cut flow of all M_X (GeV) of spin-2 bulk graviton.

category	hadron flavor of AK8 jets	hadron flavor of subjets
bb	5	5 (both)
b	5	5 (only one)
cc/c	4	4 (at least one)
light	all remaining	all remaining

TABLE 3.12: List of categorization of multijet events.

3.6 Data and Monte Carlo Comparison

In the section, the comparison of Monte Carlo simulations of background and data will be shown to demonstrate the domiant components in data. Multi-jet events are added up by samples of different H_T section listed in table 3.4, and seperated into four categories summarized in the table 3.10. Besides, the cross sections at leading order of multi-jet events are multiplied by a factor about 0.7 to modify them closer to the value of next leading order.

- Pile-up re-weighting: all selection is used except τ_{21} and double-b tagger. The weighting procedure is described in chapter 2.2.

- Inverse double-b region : all selection is used except only one of double-b taggers passing the loose criteria.

- Inverse τ_{21} region: all selection is used except only one of τ_{21} passing the criteria of 0.55.

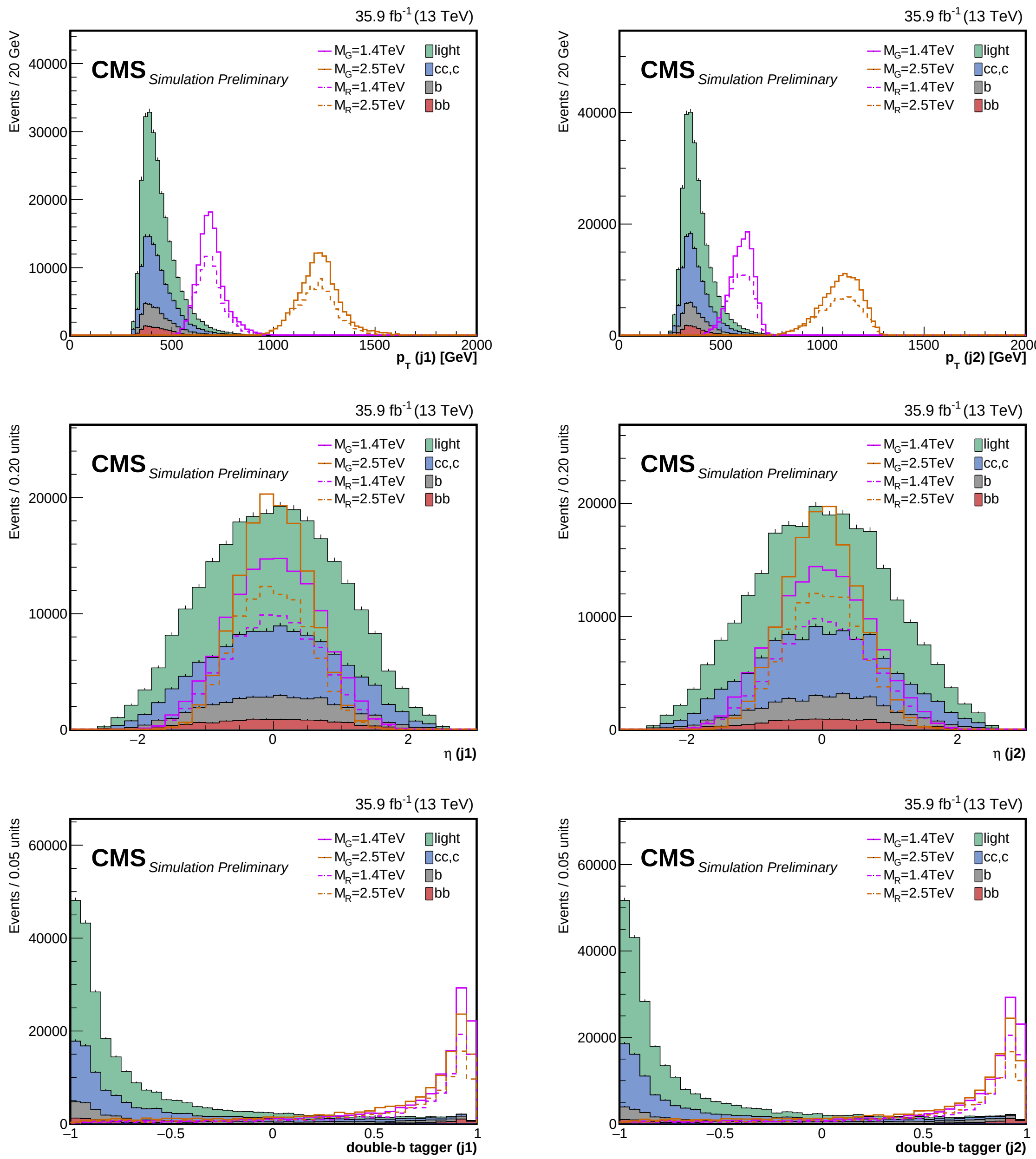

FIGURE 3.2: The comparison of signal and background. The signals of M_X = 1.4 TeV and 2.5 TeV from both models are shown. The cross section is set to 20 pb in the figures. Multi-jet events are seperated into four categories summarized in the table 3.10. From top to buttom are the comparison of p_T, η, and double-b tagger of leading (left) and next leading (right) AK8 jet.

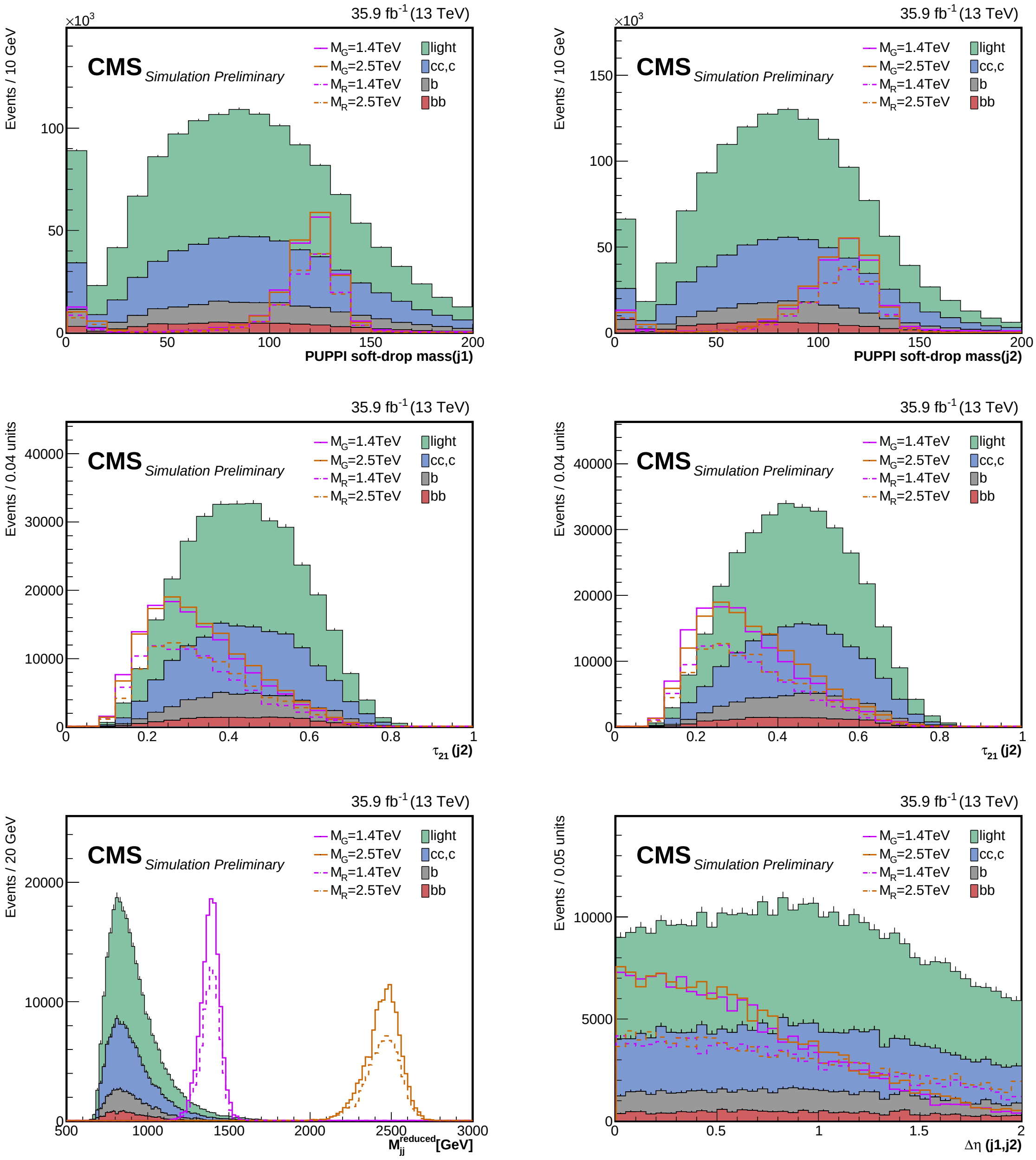

FIGURE 3.3: The comparison of signal and background. The signals of $M_X = 1.4$ TeV and 2.5 TeV from both models are shown. The cross section is set to 20 pb in the figures. Multi-jet events are seperated into four categories summarized in the table 3.10. From top to buttom are the comparison of PUPPI soft-drop mass, τ_{21} of leading (left) and next leading (right) AK8 jet, the reduced mass (buttom left), and $|\Delta\eta$ (the two leading AK8 jets)$|$ (buttom right).

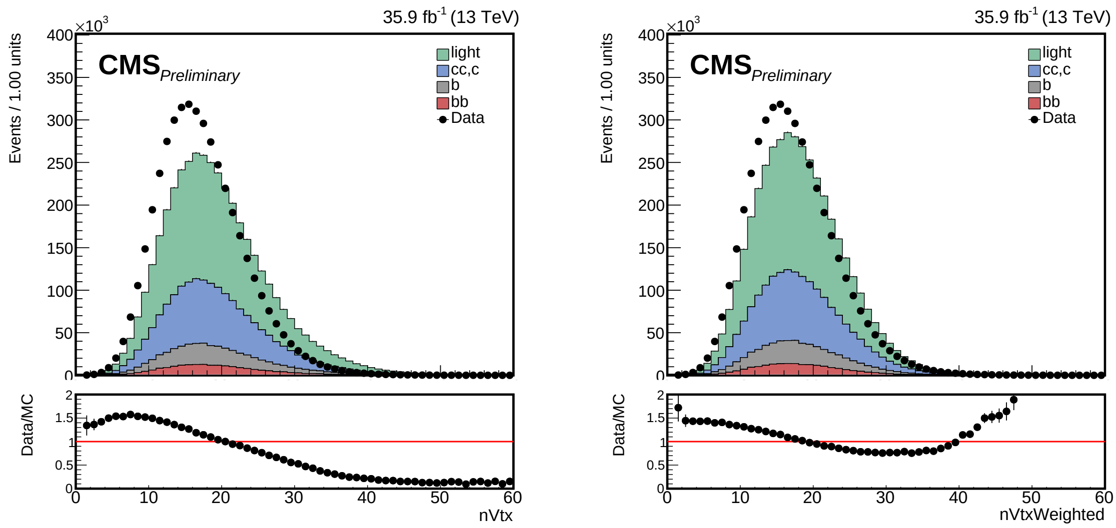

FIGURE 3.4: The comparison of data and background of pile-up distribution with (left) and without (right) pile-up re-weighting. Multi-jet events are seperated into four categories summarized in the table 3.10.

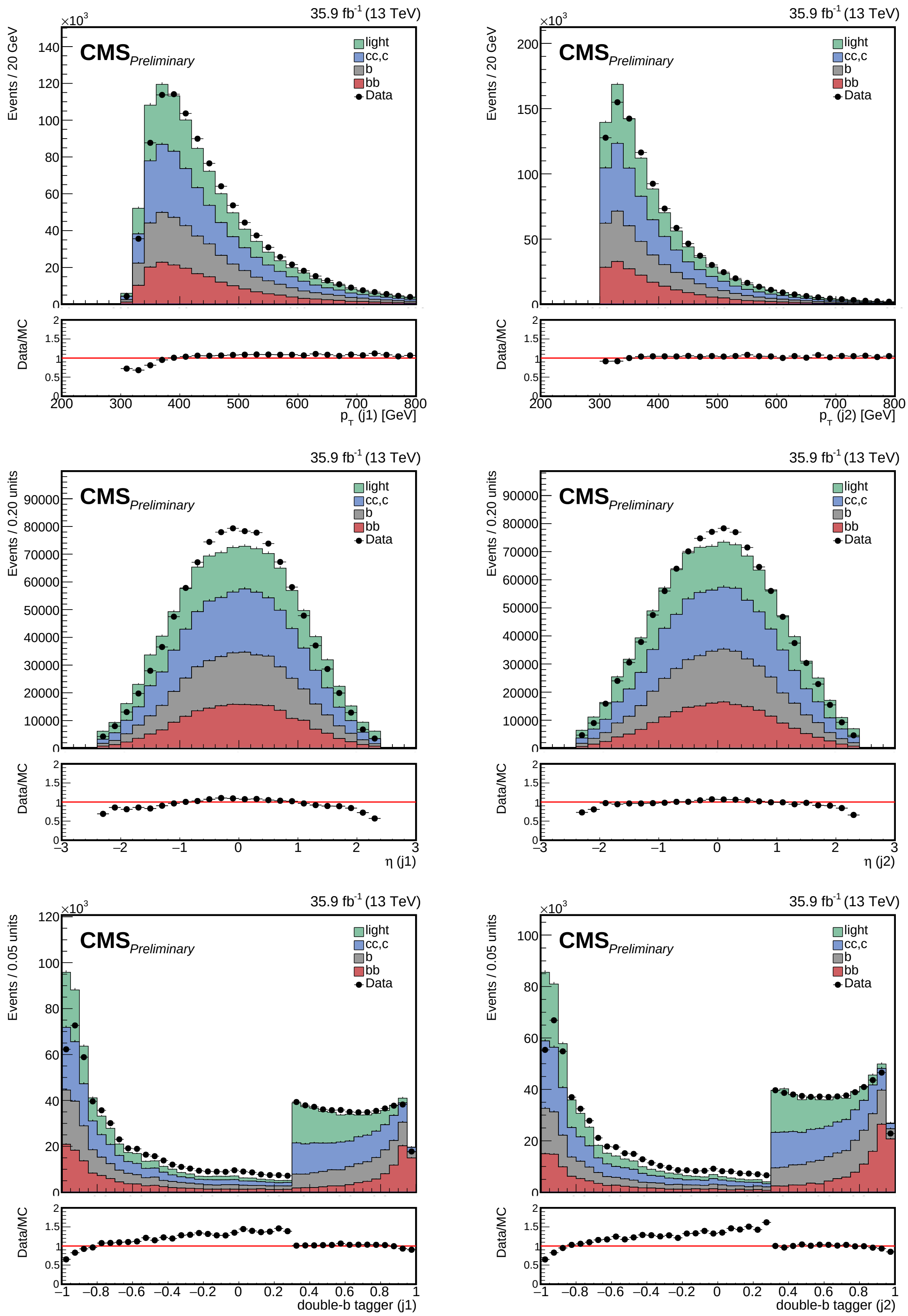

FIGURE 3.5: The comparison of data and background in inverse double-b region. Multi-jet events are seperated into four categories summarized in the table 3.10. From top to buttom are the comparison of p_T, η, and double-b tagger of leading (left) and next leading (right) AK8 jet.

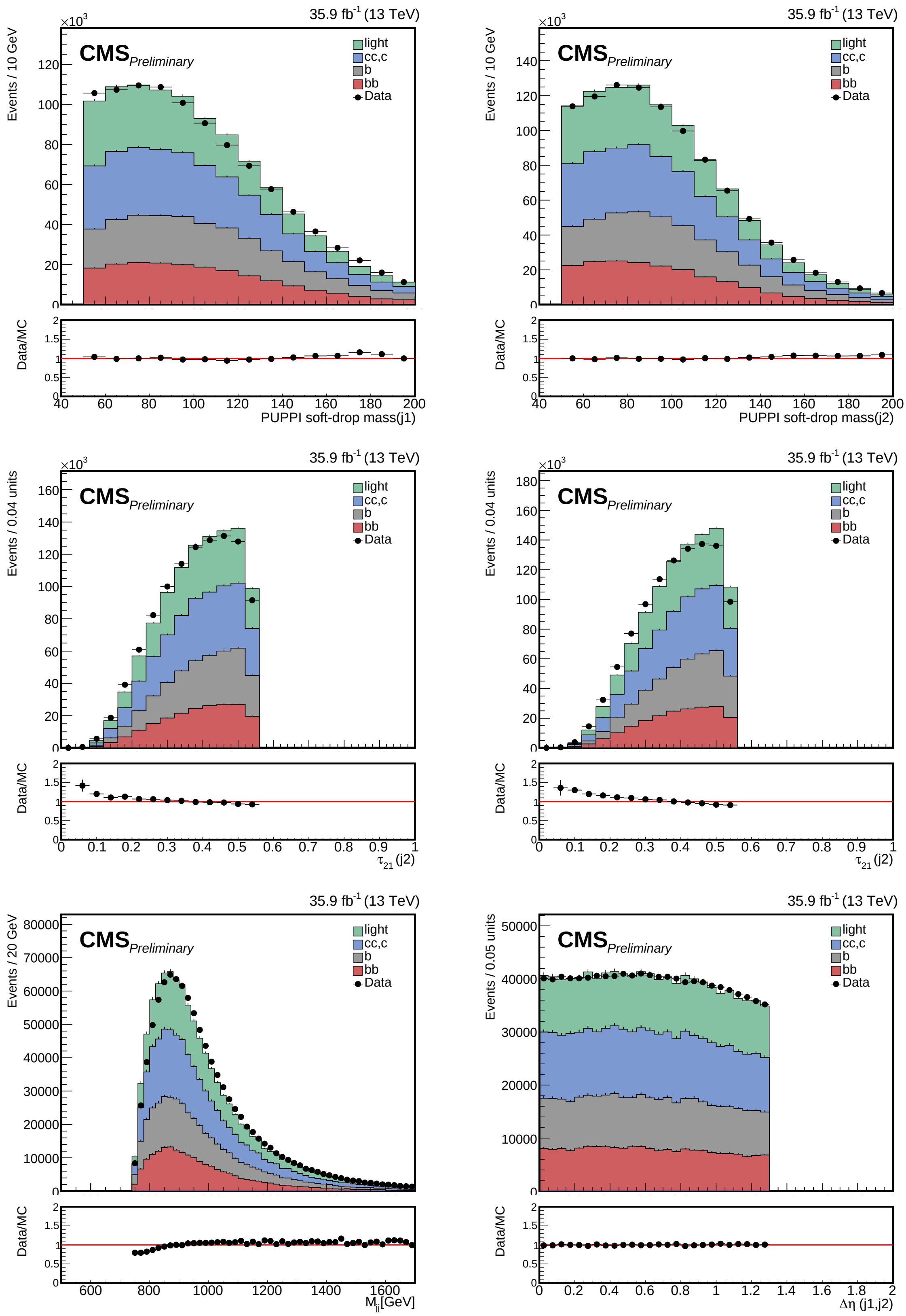

FIGURE 3.6: The comparison of data and background in inverse double-b region. Multi-jet events are seperated into four categories summarized in the table 3.10. From top to buttom are the comparison of PUPPI soft-drop mass, τ_{21} of leading (left) and next leading (right) AK8 jet, the reduced mass (buttom left), and $|\Delta\eta$ (the two leading AK8 jets)$|$ (buttom right).

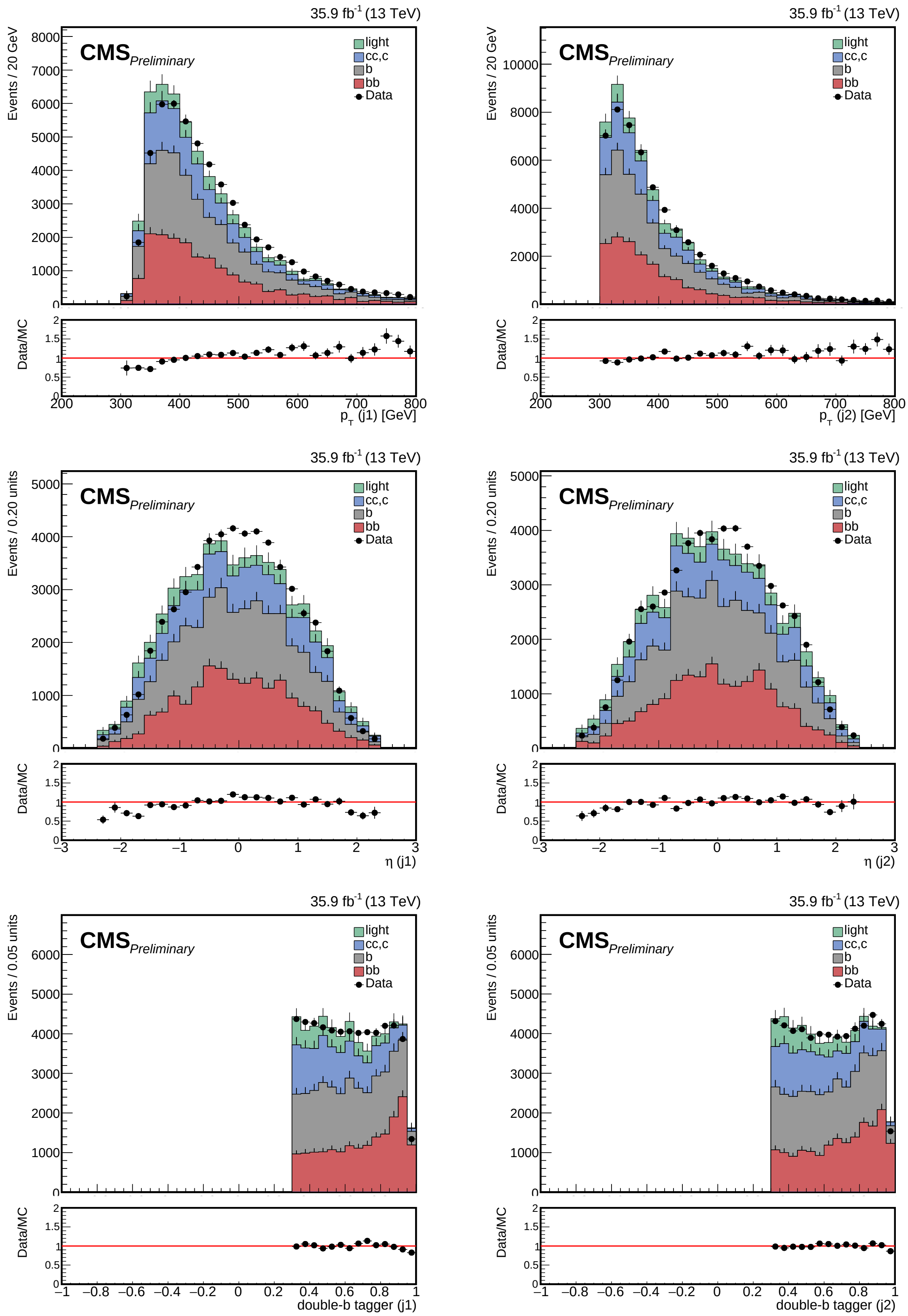

FIGURE 3.7: The comparison of data and background in inverse τ_{21} region. Multi-jet events are seperated into four categories summarized in the table 3.10. From top to buttom are the comparison of p_T, η, and double-b tagger of leading (left) and next leading (right) AK8 jet.

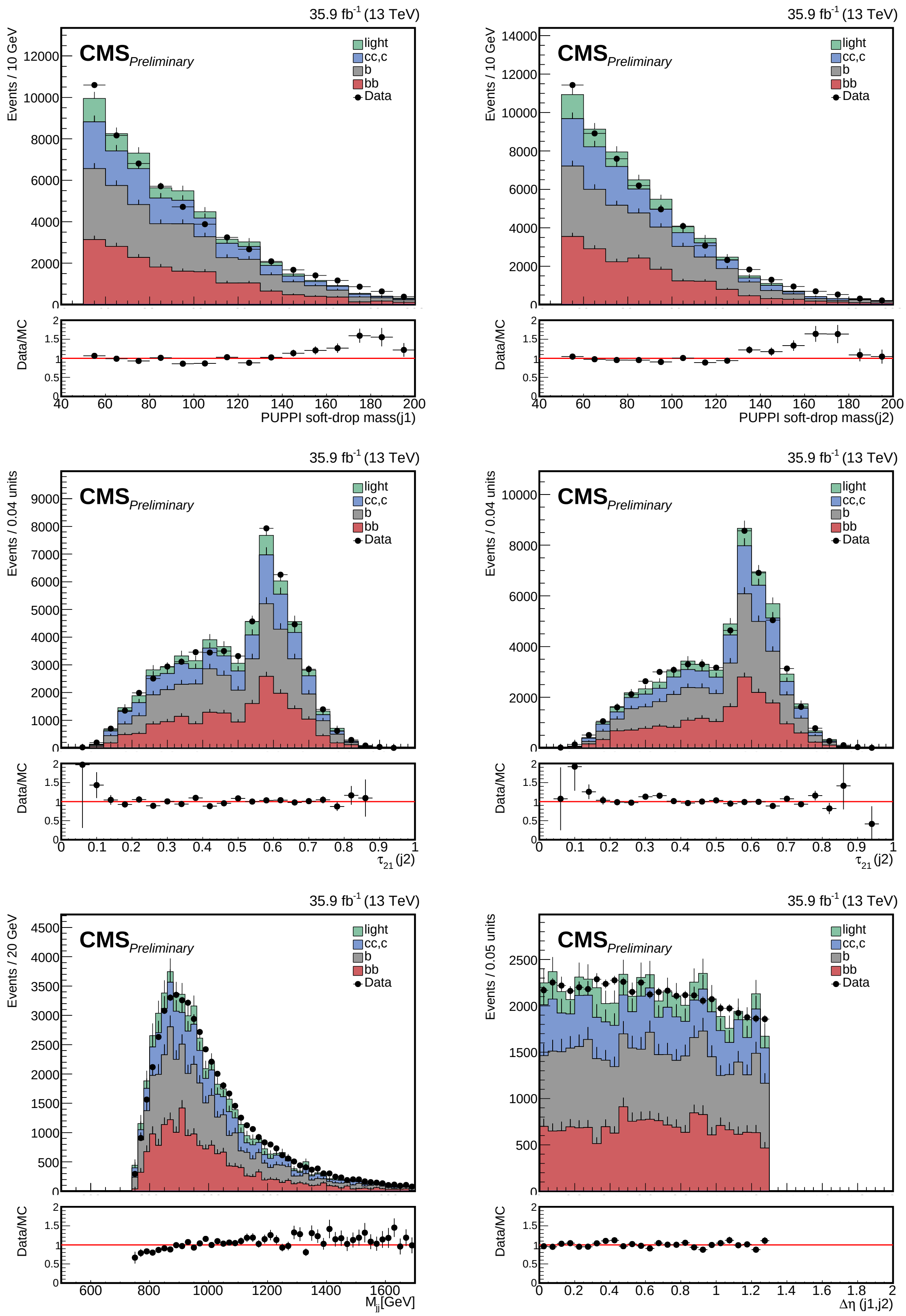

FIGURE 3.8: The comparison of data and background in inverse τ_{21} region. Multi-jet events are seperated into four categories summarized in the table 3.10. From top to buttom are the comparison of PUPPI soft-drop mass, τ_{21} of leading (left) and next leading (right) AK8 jet, the reduced mass (buttom left), and $|\Delta\eta$ (the two leading AK8 jets)$|$ (buttom right).

Chapter 4

Background Estimation

In this channel whose final state are four b-flavor jets, main background contribution comes from multi-jet events. The background estimation in the study combines two method used in 2015 research: alphabet and bump hunt into alphabet assisted bump hunt.

4.1 Bump Hunt

The concept of searches for heavy resonance can be seen directly as finding a bump on the top of the smooth background, which is shown in figure 4.1. The fitted target is the mass spectrum of heavy resonances. The prababilty density function used in fitting are level-exponential function for data and Gaussian for signal.

4.2 Alphabet

Alphabet method evoled from ABCD method which assumes the background is homogenously distributed on the two-dimension histogram. The histogram is sepearted into signal region and sideband region. The background in signal region can be extrapolated from sideband region. For example, if we see the

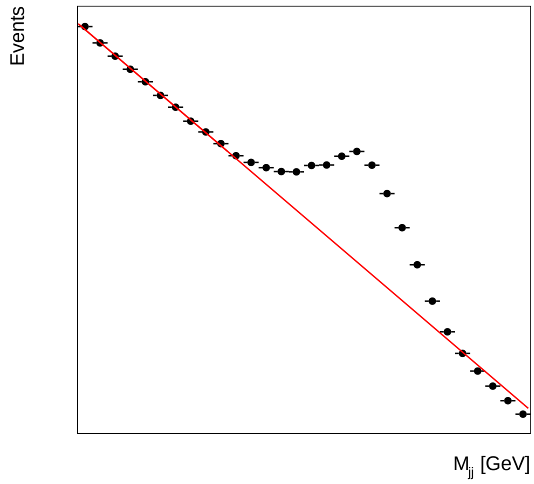

FIGURE 4.1: The cartoon of a bump on the background.

figure 4.2, the number of events in signal region can get by:

$$\begin{aligned} \frac{N_{signal}}{N_{anti-tag}} &= \frac{N_{sidebandB}}{N_{sidebandA}} = \frac{N_{sidebandD}}{N_{sidebandC}}, \\ N_{signal} = \frac{N_{sidebandB} \times N_{anti-tag}}{N_{sidebandA}} &= \frac{N_{sidebandD} \times N_{anti-tag}}{N_{sidebandC}} \\ &= N_{anti-tag} \times R_{p/f}, \end{aligned} \tag{4.1}$$

where N is the number of events located in the square region. The ratio $\frac{N_{signal}}{N_{anti-tag}}$ is referred as $R_{p/f}$ in the section. If the $R_{p/f}$ has dependence on the mass of the leading AK8 jet, one should use Alphabet method instead of ABCD method, as figure 4.3 and 4.4 show. Alphabet method gives $R_{p/f}$ a dependence on the mass of the leading AK8 jet:

$$N_{signal} = N_{anti-tag} \times R_{p/f}(M_{leadingAK8}). \tag{4.2}$$

The $R_{p/f}$ is derived in each bin of the mass of leading AK8 jet in mass side band. All $R_{p/f}$ of each bin is fitted together by a quadratic polynominal fit to interpolate the $R_{p/f}$ in the region of mass of signal. The fit results are shown in figure 4.4. Finally, the predicted background is get from an anti-tagged event weighted according to the mass of its leading AK8 jet. Figure 4.5 is predicted background

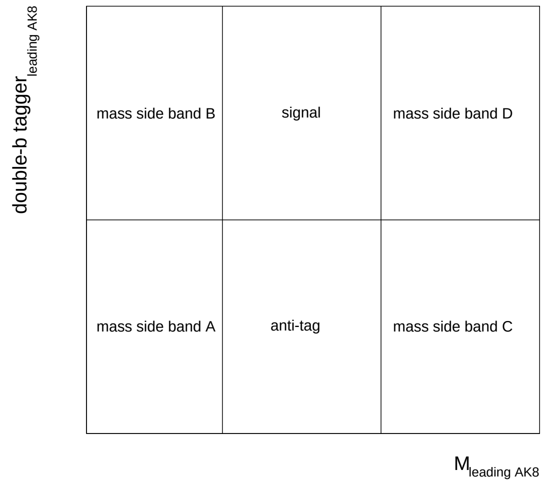

FIGURE 4.2: The cartoon of a two dimensional distribution.

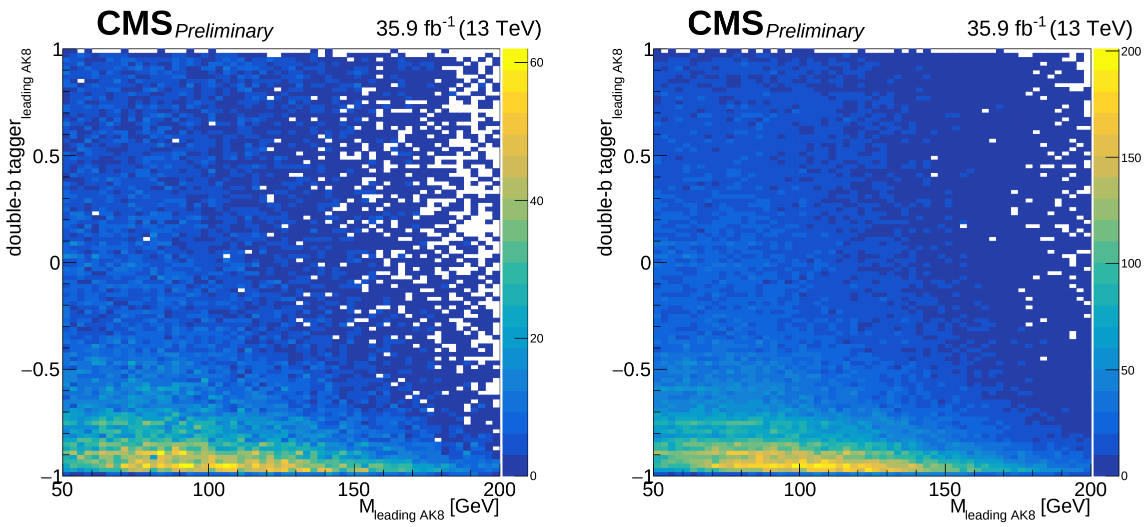

FIGURE 4.3: The double-d tagger versus the mass of the leading AK8 jet distribution in TT (left) and LL (right) region.

in both LL and TT region.

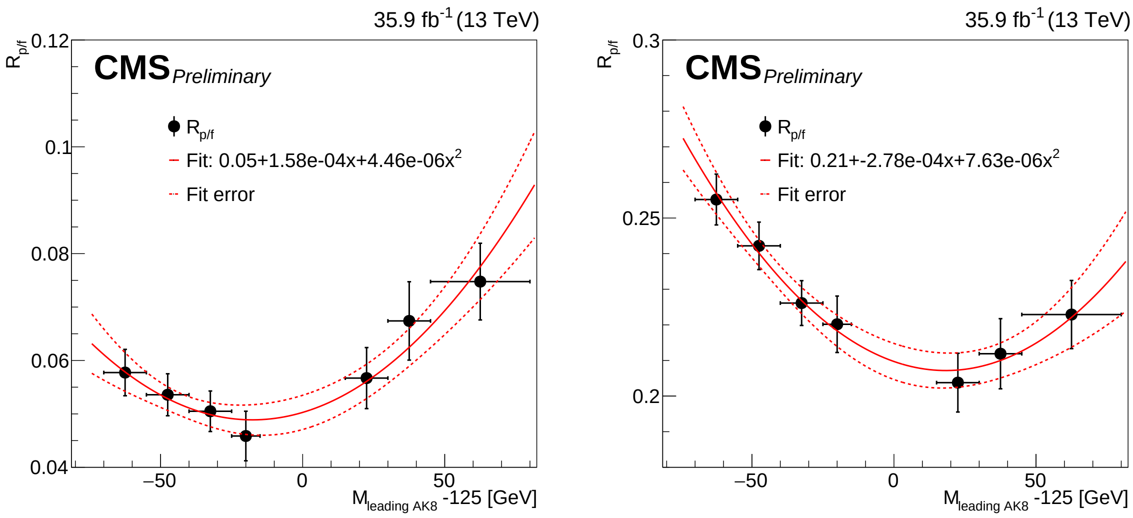

FIGURE 4.4: The $R_{p/f}$ and its quadratic fit in TT (left) and LL (right) region.

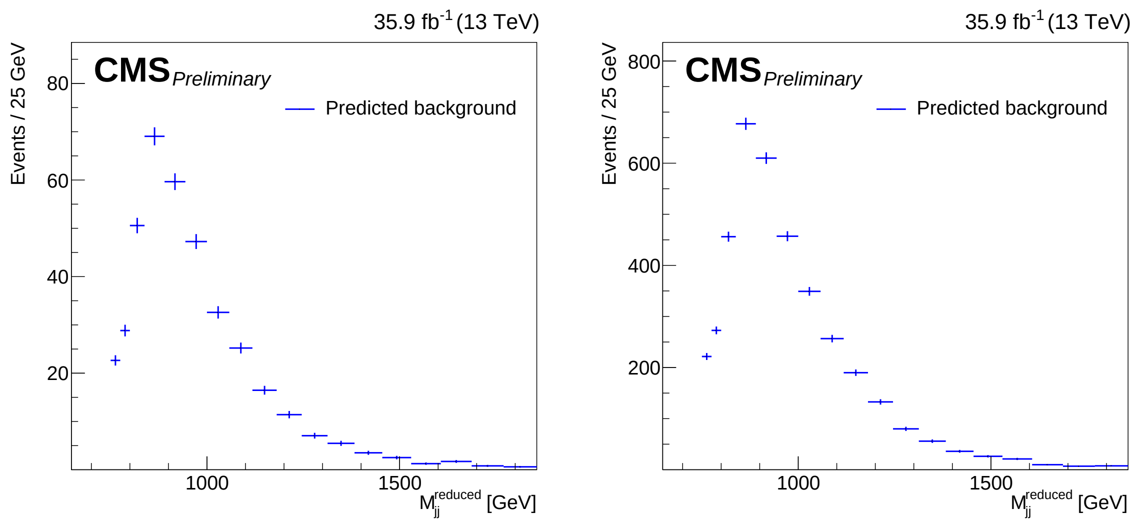

FIGURE 4.5: The $R_{p/f}$ and its quadratic fit in TT (left) and LL (right) region.

4.3 Alphabet Assisted Bump Hunt

The two background estimation methods, alphabet and bump hunt, use orthogonal information from data. While bump hunt drive in signal region, alphabet extrapolate from data in side band region. Therefore, we can combine two method into alphabet assisted bump hunt.

The estimation is inplemented as follow:

- Define a tagging and anti-tagging region. the double-b tagger working point is used as a discriminator here.
- Derive the ratio of number of events in tagging region to that of anti-tagging region, which referred below "$R_{p/f}$".
- The dependence of $R_{p/f}$ on M_{jj} and that on $M_{HiggsJet}$ are considered, while the latter is small enough to be ignored. The shape and the numbner of estimated background can be get from:

$$Bkg(M_{jj}) = R_{p/f}(M_{jj}) \times Anti - tag(M_{jj}), \tag{4.3}$$

  which can be further reduced to

$$\begin{aligned} R_{p/f}(M_{jj}) &= 1 + (M_{jj} \times lin_{par}) \\ Bkg(M_{jj}) &= (1 + (M_{jj} \times lin_{par})) \times Anti - tag(M_{jj}), \end{aligned} \tag{4.4}$$

  where the parameters in Bkg(M_{jj}) are initialized the same as Anti-tag(M_{jj}), and lin_{par} is a parameter of the linear dependence on M_{jj}

- The function Bkg(M_{jj}) fits on the data in signal region to finish a post-fit procedure.